

Hyperbolic Spin Liquids

Patrick M. Lenggenhager^{1,*}, Santanu Dey^{1,2,3}, Tomáš Bzdušek^{1,4}, and Joseph Maciejko^{1,2,5,†}

¹*Max Planck Institute for the Physics of Complex Systems, Nöthnitzer Str. 38, 01187 Dresden, Germany*

²*Department of Physics, University of Alberta, Edmonton, Alberta T6G 2E1, Canada*

³*Laboratoire de Physique de l'École normale supérieure, ENS, Université PSL, CNRS, Sorbonne Université, Université Paris Cité, F-75005 Paris, France*

⁴*Department of Physics, University of Zürich, Winterthurerstrasse 190, 8057 Zürich, Switzerland*

⁵*Theoretical Physics Institute & Quantum Horizons Alberta, University of Alberta, Edmonton, Alberta T6G 2E1, Canada*



(Received 19 July 2024; revised 19 December 2024; accepted 7 July 2025; published 15 August 2025)

Hyperbolic lattices present a unique opportunity to venture beyond the conventional paradigm of crystalline many-body physics and explore correlated phenomena in negatively curved space. As a theoretical benchmark for such investigations, we extend Kitaev's spin-1/2 honeycomb model to hyperbolic lattices and exploit their non-Euclidean space-group symmetries to solve the model exactly. We elucidate the ground-state phase diagram on the $\{8, 3\}$ lattice and find a gapped \mathbb{Z}_2 spin liquid with Abelian anyons, a gapped chiral spin liquid with non-Abelian anyons and chiral edge states, and a Majorana metal whose finite low-energy density of states is dominated by non-Abelian Bloch states.

DOI: 10.1103/s25y-s4fj

Introduction—Among the factors that influence the collective behavior of quantum materials, lattice geometry plays a crucial role, from determining the electronic band structure for weak correlations to geometrically frustrating conventional orders for strong correlations [1]. Hyperbolic $\{p, q\}$ lattices [2–8]—synthetic materials that emulate regular tilings of two-dimensional (2D) hyperbolic space by p -sided polygons with coordination q , with $(p - 2)(q - 2) > 4$ [9]—present a unique opportunity to explore many-body physics in unusual, non-Euclidean lattice geometries. While a wealth of phenomena have been investigated on hyperbolic lattices at the single-particle level [10–42], much less is known about the interplay of negative curvature and many-body correlations.

Hyperbolic analogs of prototypical interacting Hamiltonians such as the quantum Ising, XY, and Heisenberg models [43–45] and the Bose [46] and Fermi [45,47,48] Hubbard models have been studied recently using mean-field theory, spin-wave theory, and quantum Monte Carlo (QMC). However, the ability of such methods to reliably capture the bulk properties of hyperbolic lattices must be critically assessed. For example, finite $\{10, 3\}$ lattices display a low-energy density of states

(DOS) that appears semimetallic [45,47], but the thermodynamic-limit DOS is known to be finite [24], with important consequences for many-body physics. Thus, even numerically exact methods such as QMC may suffer from unusually severe finite-size effects in the hyperbolic context. This motivates a search for exactly solvable models, to not only discover interesting emergent phenomena but also benchmark approximate many-body theories of hyperbolic lattices.

Here, we introduce for the first time an exactly solvable model of strongly correlated spins on hyperbolic lattices (Fig. 1). Our model generalizes Kitaev's honeycomb lattice model [49] to $\{p, 3\}$ lattices and can be solved exactly for any even $p \geq 8$. Although the Kitaev model can be generalized to arbitrary three-coordinated graphs, exact solvability does not immediately follow. First, a three-edge coloring of the graph must exist and be explicitly constructed, which is in general an NP-complete problem [50]. Second, even with conserved plaquette fluxes [49], the flux optimization problem is generically hard because of the exponential growth of flux configurations with system size. While Lieb's lemma [51–55] can simplify the problem if reflection symmetries are present, unlike Euclidean lattices, noncrystalline structures typically possess at most finitely many such symmetries, thus exponentially many flux configurations must still be sampled numerically [56,57]. Here, we resolve both issues by exploiting the space-group symmetries of hyperbolic lattices [11,19,20]. First, infinitely many non-Euclidean reflection symmetries allow us to simultaneously solve the three-edge coloring problem and determine the ground-state flux configuration analytically. Second, the (noncommutative) translation symmetry

*Contact author: plengg@pks.mpg.de

†Contact author: maciejko@ualberta.ca

Published by the American Physical Society under the terms of the [Creative Commons Attribution 4.0 International license](#). Further distribution of this work must maintain attribution to the author(s) and the published article's title, journal citation, and DOI. Open access publication funded by the Max Planck Society.

enables us to efficiently approximate the thermodynamic limit via hyperbolic band theory (HBT) [11–13]. We study the model at zero temperature on the $\{8, 3\}$ lattice and find two gapped topological phases: a \mathbb{Z}_2 spin liquid with Abelian anyons, and a chiral spin liquid with non-Abelian anyons and chiral Majorana edge modes. Around the isotropic point in the phase diagram, we also find a Majorana metal which—unlike Kitaev’s Dirac spin liquid [49]—has a finite low-energy DOS dominated by non-Abelian Bloch states [12].

Hyperbolic Kitaev model—We consider hyperbolic $\{p, 3\}$ lattices with a three-edge coloring, i.e., an assignment of one of three colors (yellow, red, blue, labeled as $\alpha = x, y, z$, respectively) to each edge such that coincident edges have different colors [Fig. 1(a)]. With an $s = 1/2$ spin on each site, we define the ferromagnetic ($J_\alpha > 0$) hyperbolic Kitaev model (HKM) as

$$\hat{\mathcal{H}} = - \sum_{\langle j, k \rangle_\alpha} J_\alpha \hat{\sigma}_j^\alpha \hat{\sigma}_k^\alpha - K \sum_{[lmn]_{\alpha\beta\gamma}^+} \epsilon_{\alpha\beta\gamma} \hat{\sigma}_l^\alpha \hat{\sigma}_m^\beta \hat{\sigma}_n^\gamma. \quad (1)$$

The J_α term is an anisotropic exchange interaction between adjacent sites j, k sharing an α edge $\langle j, k \rangle_\alpha$. The term involving the totally antisymmetric tensor $\epsilon_{\alpha\beta\gamma}$ is an interaction among a counterclockwise-oriented triplet of sites n, m, l (denoted $[lmn]_{\alpha\beta\gamma}^+$) that are connected by bonds $\langle l, m \rangle_\alpha$ and $\langle m, n \rangle_\gamma$, respectively, with $\beta \neq \alpha, \gamma$ the color of

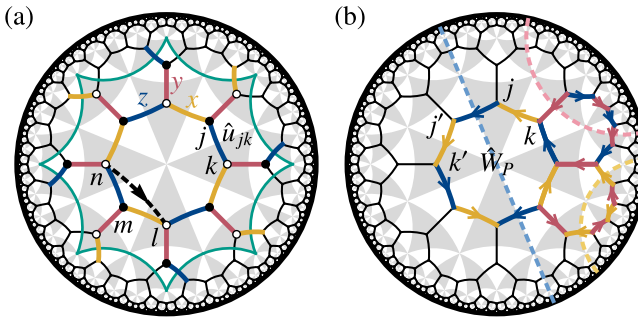


FIG. 1. (a) Hyperbolic Kitaev model on the $\{8, 3\}$ lattice with two sublattices (white and black dots). Symmetric three-edge coloring (yellow, red, and blue, representing x, y , and z) shown inside the primitive cell (green octagon with opposite edges identified). Adjacent sites j, k form a bond $\langle j, k \rangle_\alpha$; sites n, m, l form an oriented triplet $[lmn]_{xyz}^+$. In the Majorana representation, these generate the bond operator \hat{u}_{jk} and a next-nearest-neighbor term (dashed black arrow), respectively. The symmetry of the model is depicted by the gray or white triangles. (b) Application of Lieb’s lemma to determine the ground-state flux sector for three representative plaquettes. Three independent mirror lines (dashed geodesics) cut bonds of a different color. Separately for each plaquette, reflection positivity with respect to one of them implies ground-state bond eigenvalues $u_{jk} = +1$ as indicated by arrows from k to j (up to gauge transformations). This constrains the gauge-invariant plaquette operators \hat{W}_P consistently throughout the lattice: here $W_P = -1$ for all P .

the third bond adjacent to site m . This term can arise as the leading-order nontrivial effect of a perturbation $-\sum_{j,\alpha} h_\alpha \hat{\sigma}_j^\alpha$ by an external magnetic field \mathbf{h} [49], or through Floquet engineering [58].

Not all graphs are three-edge colorable, but any three-coordinated *bipartite* simple graph is according to König’s theorem [59]. Although this applies to any infinite $\{p, 3\}$ lattice with even p , such a coloring is not unique. In Appendix A, we describe an algorithm for constructing a three-edge coloring for any hyperbolic $\{p, 3\}$ lattice with p even [see Fig. 1(a) for $p = 8$] such that Eq. (1) is symmetric with respect to any (non-Euclidean) bond-cutting reflection, of which there are three types [Fig. 1(b)]. The coloring is also compatible with translation symmetry and appropriately chosen periodic boundary conditions (PBC), and can be seen as a hyperbolic generalization of the Kekulé pattern on the honeycomb lattice [60].

Majorana representation—We now solve the HKM exactly. At each site j , we introduce the Majorana fermions \hat{b}_j^α , $\alpha \in \{x, y, z\}$ and \hat{c}_j such that $\hat{\sigma}_j^\alpha = i\hat{b}_j^\alpha \hat{c}_j$ [49]. Defining the bond operator $\hat{u}_{jk} = i\hat{b}_j^\alpha \hat{b}_k^\alpha$ on edge $\langle j, k \rangle_\alpha$, the Hamiltonian becomes [49,61]

$$\hat{\mathcal{H}} = \sum_{\langle j, k \rangle_\alpha} J_\alpha \hat{u}_{jk} i\hat{c}_j \hat{c}_k + K \sum_{[lmn]_{\alpha\beta\gamma}^+} \hat{u}_{lm} \hat{u}_{mn} i\hat{c}_l \hat{c}_n. \quad (2)$$

While $\hat{\mathcal{H}}$ in Eq. (2) acts on the extended Hilbert space, $\hat{\mathcal{H}}$ in Eq. (1) only acts on the physical Hilbert space of the spin system, defined as the common $+1$ eigenspace of the \mathbb{Z}_2 gauge transformations $\hat{D}_j = \hat{b}_j^x \hat{b}_j^y \hat{b}_j^z \hat{c}_j$.

Because the \hat{u}_{jk} commute with $\hat{\mathcal{H}}$ and each other, we replace them by their eigenvalues $u_{jk} = \pm 1$ and study the resulting quadratic Majorana Hamiltonian. Since the bond operators are not gauge invariant, we consider the Wilson loops $\hat{W}(\ell) = \prod_{\langle j, k \rangle_\alpha \in \ell} \hat{\sigma}_j^\alpha \hat{\sigma}_k^\alpha$ along closed paths ℓ . In the Majorana representation, they take the form $\hat{W}(\ell) = \prod_{\langle j, k \rangle_\alpha \in \ell} (-i\hat{u}_{jk})$. On an infinite hyperbolic lattice, all u_{jk} are (up to gauge transformations) fully determined by the Wilson loops \hat{W}_P around the individual plaquettes P , measuring the corresponding flux. On compactified PBC clusters with genus g , plaquette fluxes can only be changed in pairs, and there also exist Wilson loops along $2g$ noncontractible paths [22].

Exact solution of the flux problem—For $K = 0$, the ground-state configuration of plaquette fluxes can be determined analytically from symmetry. First, Lieb’s lemma on reflection positivity [51–55] implies that, in the ground state, the gauge variables \hat{u}_{jk} lying on either side of a mirror line are related by reflection, up to gauge transformations. Since our model is reflection symmetric with respect to *any* bond-cutting mirror line for *any* choice of parameters J_α [Fig. 1(b)], we can consider each plaquette separately.

Given a plaquette, we select one of the reflection symmetries and denote by j' the image of site j under that reflection. We can always choose a gauge where $u_{j'j} = +1$ for the bonds crossing the mirror line [dashed geodesics in Fig. 1(b)]. Then, Lieb's lemma implies that the remaining reflection-related bonds satisfy $u_{jk} = u_{k'j'}$. Indeed, under reflection symmetry the term $u_{jk}\hat{c}_j\hat{c}_k$ is mapped to $u_{jk}(-i)\hat{c}_{j'}\hat{c}_{k'} = u_{jk}i\hat{c}_{k'}\hat{c}_{j'}$ (reflection is represented anti-unitarily for Majorana fermions). Thus, for a $\{p, 3\}$ lattice with p even,

$$W_P = (-i)^p \times (-1) \times (+1)^{p/2-1} = -(-1)^{p/2}, \quad (3)$$

where $(-i)^p$ follows from the definition of W_P , (-1) from the opposite orientation (relative to the oriented Wilson loop) of the two bonds cut by the mirror line, and $(+1)^{p/2-1}$ from the remaining $(p/2-1)$ reflection-related pairs of bonds each having equal orientation. Unlike in the case of the coloring studied traditionally [49], Eq. (3) applies for any choice of couplings J_α .

The honeycomb $\{6, 3\}$ lattice has $p/2 = 3$, such that $W_P = +1$, while in our example, $p/2 = 4$, thus the ground state has homogeneous π flux ($W_P = -1$). By further exploring all $2^{6-1} = 32$ possible translation-invariant flux configurations on the infinite $\{8, 3\}$ lattice, we find that, in agreement with Eq. (3), the homogeneous π -flux configuration results in the lowest many-fermion ground-state energy, see Appendix D. For concreteness, we subsequently focus on the $\{8, 3\}$ lattice.

Fermionic spectrum—Having determined the ground-state flux sector, we next study the spectrum of fermionic excitations as a function of the couplings J_α . The relevant quadratic Majorana Hamiltonian $\hat{\mathcal{H}} = (i/4) \sum_{j,k} A_{jk} \hat{c}_j \hat{c}_k$ possesses hyperbolic translation symmetry, thus we diagonalize it using HBT [11–13]. To capture the non-Abelian Bloch states [12] characteristic of hyperbolic reciprocal space, we generalize the supercell method [13] to quadratic Majorana Hamiltonians, see Appendix B. We use a coherent sequence [13,25,26] of five supercells containing up to 2048 sites, obtained from HYPERCELLS [13,81–83], and perform random sampling of momenta using HYPERBLOCH [84]. From the fermionic spectrum, we deduce the DOS $\rho(E)$ and corresponding spectral gap ΔE as described in Appendix C. To complement the supercell method based on HBT, we additionally compute $\rho(E)$ at selected points in the phase diagram using the real-space continued-fraction method [24,85,86] on PBC clusters and finite flakes with open boundary conditions (OBC) containing $\sim 10^8$ sites [61].

Majorana metal—We first consider the case $K = 0$. The ΔE phase diagram in Fig. 2(a) shows a gapless phase (M) around the isotropic point $J_x = J_y = J_z$ (see inset) and a gapped phase away from it (G). Representative DOS computed from different methods are in excellent

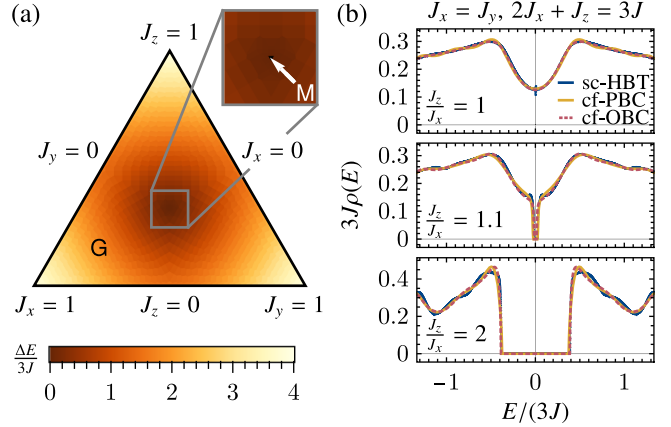


FIG. 2. (a) Phase diagram of the spectral gap ΔE for $K = 0$ in the plane $J_x + J_y + J_z = 3J$. Inset: region near the isotropic point ($J_x = J_y = J_z = J$) where the gap vanishes (black), separating a Majorana metal (M), from the gapped (G) spin-liquid phase. (b) Low-energy fermionic DOS (top) at the isotropic point, (middle) slightly away from it, and (bottom) deep in the anisotropic region, calculated using the supercell method (sc-HBT; 2048 sites) and the continued-fraction method applied to clusters with periodic (cf-PBC) and to flakes with open boundary conditions (cf-OBC) with $\sim 10^8$ sites.

agreement [Fig. 2(b)]. Our data suggests the gapless phase M is confined to the isotropic point, or at most a small region around it [Fig. 3(b)]. The phase is characterized by a finite DOS at $E = 0$ in sharp contrast to the linearly vanishing DOS $\rho(E) \propto |E|$ associated with the Dirac spectrum on the honeycomb lattice [49]. Thus, unlike Kitaev's Dirac spin liquid, the $\{8, 3\}$ HKM realizes a *Majorana metal*. Crucially, Abelian HBT alone incorrectly predicts a vanishing DOS $\rho(E) \propto |E|^3$ at low energies arising from conical singularities in the 4D Brillouin zone of Abelian Bloch states. However, the latter only capture particular slices through the full reciprocal space which is dominated by non-Abelian Bloch states [18]. Thus, the finite DOS here is a direct consequence of non-Abelian Bloch physics, which is absent for Euclidean lattices. Similar phenomenology, where non-Abelian Bloch states drastically alter the low-energy DOS, has been observed in Ref. [34].

\mathbb{Z}_2 spin liquid—To better understand the nature of the gapped (G) phase away from the isotropic point, we study the HKM in the limit of extreme coupling anisotropy, $J_x, J_y \ll J_z$, where the fermion gap $\Delta E/(3J) \approx 4$ [Fig. 2(a)]. When $J_x = J_y = 0$, the model reduces to decoupled Ising dimers on z-bonds, each of which minimizes its energy by adopting one of two ferromagnetic configurations ($\uparrow\downarrow$ or $\downarrow\uparrow$), resulting in a macroscopic ground-state degeneracy. This degeneracy is lifted at small but nonzero J_x, J_y , and the nature and spectrum of the resulting low-energy excitations can be determined from an effective Hamiltonian obtained by degenerate perturbation

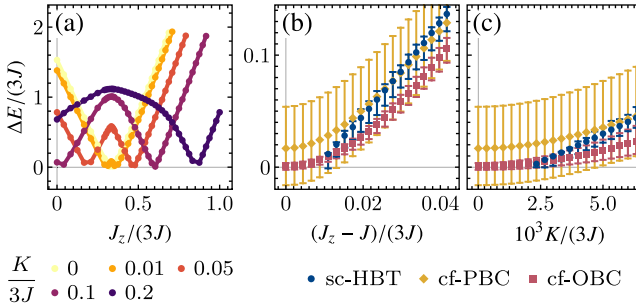


FIG. 3. Spectral gap ΔE as a function of J_z and K . (a) Vertical cut through the phase diagram in Fig. 2(a) for different values of K (see legend below panel), with $J_x = J_y = (3J - J_z)/2$. (b) Close-up of (a) for $K = 0$ showing the gap opening as a function of J_z obtained using the three methods (see legend below panels and caption of Fig. 2). (c) Gap opening with K at the isotropic point $J_x = J_y = J_z = J$.

theory [49,87,88]. We first find that the HKM on the $\{8, 3\}$ lattice maps exactly onto a model of effective spin-1/2 degrees of freedom and hardcore bosons on the Archimedean $(8, 4, 8, 4)$ lattice. The latter is the lattice obtained by collapsing the z -bond dimers into effective sites, and contains alternating square (\square) and octagonal (\circlearrowright) plaquettes. The spin states represent the two ferromagnetic configurations of each dimer, and bosons correspond to excitations out of the low-energy ferromagnetic subspace, with large energy cost $\Delta E/2 \approx 2J_z$.

To focus on the low-energy physics, we project onto the zero-boson subspace, and obtain the effective spin-1/2 Hamiltonian [61]:

$$\hat{\mathcal{H}}_{\text{eff}} = \frac{5}{16} \frac{J_{\parallel}^4}{J_z^3} \sum_{\square} \hat{W}_{\square} + \frac{5}{2048} \frac{J_{\parallel}^8}{J_z^7} \sum_{\circlearrowright} \hat{W}_{\circlearrowright}, \quad (4)$$

where \hat{W} are Wilson loop operators on the $(8, 4, 8, 4)$ lattice, and we have set $J_x = J_y = J_{\parallel}$ here for simplicity. The \hat{W} operators all commute with each other, and are in fact equivalent to the plaquette operators \hat{W}_P introduced earlier. Thus, the positive couplings in Eq. (4) imply that $\hat{W}_P = -1$ in the ground state, consistent with the exact result Eq. (3). Second, Eq. (4) implies that the lowest-energy excitation is a \mathbb{Z}_2 vortex with $\hat{W}_{\circlearrowright} = +1$ and energy cost $\sim J_{\parallel}^8/J_z^7$, much less than the fermion gap $\Delta E/2 \approx 2J_z$ in that limit. Finally, the effective model (4) can be further mapped to a hyperbolic analog of the toric code [89] on the $\{8, 4\}$ lattice, i.e., a hyperbolic surface code [90–95]. This last mapping reveals that the \square and \circlearrowright vortices obey bosonic self-statistics but are mutual semions, establishing that the \mathbf{G} phase is a topologically ordered \mathbb{Z}_2 spin liquid [96].

Chiral spin liquid—A different type of gapped spin liquid is obtained when the emergent Majorana fermions carry a nonzero Chern number. This requires time-reversal

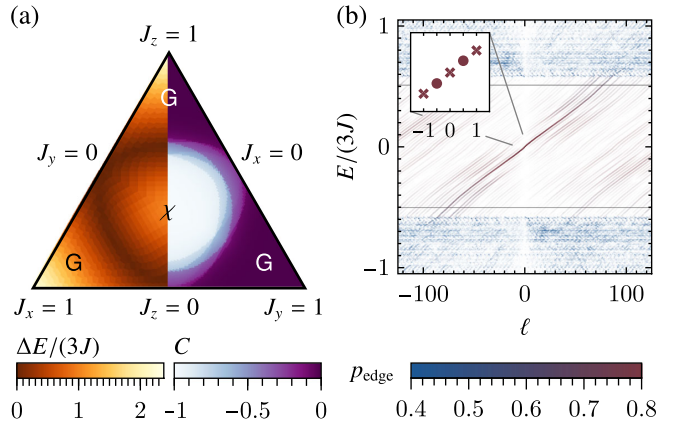


FIG. 4. (a) Phase diagram for $K/(3J) = 0.1$ with the spectral gap ΔE shown in the left half and the Chern number C computed on a PBC cluster (2048 sites) in the right half. The chiral (χ) and \mathbb{Z}_2 (\mathbf{G}) spin liquid phases are separated by a phase transition with a gap closing and an integer change in C . (b) Energy E vs angular momentum ℓ for $J_x = J_y = J_z = J$, $K/(3J) = 0.1$, computed on an OBC disk (896 sites). Color encodes the degree of edge localization p_{edge} , and opacity the weight of the corresponding ℓ . Inset: $\ell \in \mathbb{Z} + \frac{1}{2}$ (red dots) at low energies without a vortex, and $\ell \in \mathbb{Z}$ (red crosses) with a \mathbb{Z}_2 vortex at the center of the disk.

symmetry to be broken, which happens for $K \neq 0$. Focusing first on the isotropic point, where for $K = 0$ the fermionic spectrum is gapless, a gap opens at infinitesimal $K \neq 0$ and subsequently increases with increasing K [Fig. 3(c)]. Thus, for finite K , a new gapped phase χ develops around the isotropic point and remains separated from \mathbf{G} by a circular gapless line in parameter space [Fig. 4(a), left half]. From cuts through the phase diagram for different values of K [Fig. 3(a)], we find that the χ region expands with increasing K .

The Chern number C determines the properties of anyonic excitations as well as the existence and character of topologically protected boundary modes [49]. While in Euclidean translation-invariant systems, C can be easily computed in momentum space, we rely here on a real-space formulation [49] and compute it on finite PBC clusters [61]. Figure 4(a) shows that the gapped χ phase around the isotropic point has odd Chern number $C = -1$, establishing it as a chiral spin liquid with non-Abelian anyons [49], while C vanishes in the gapped \mathbb{Z}_2 spin liquid (\mathbf{G}) phase.

Finally, the nonzero Chern number suggests gapless chiral edge modes, which we investigate in a disk-shaped OBC flake at the isotropic point. For a sufficiently large flake, an approximate continuous rotation symmetry emerges on the edge, allowing us to introduce an approximate angular momentum quantum number ℓ , as discussed in Appendix E. In Fig. 4(b), we show the corresponding angular dispersion together with a measure p_{edge} of edge localization defined as the integrated probability density within the outer 10% of the hyperbolic radius of the flake. Bulk modes (blue) generally do not have sharp angular

momentum, but a branch of states sharply peaked at a single ℓ and strongly localized on the edge (red) crosses the bulk gap; we identify it with the single dispersive band of chiral edge states expected for the $C = -1$ topology. In contrast to Euclidean lattices, there is an extensive number of such edge states due to the finite boundary-to-bulk ratio in hyperbolic geometry.

For edge modes described by a chiral Majorana conformal field theory with chiral central charge $c_- = 1/2$, we expect a linear low-energy angular dispersion $E \propto \ell$ with half-integer quantization $\ell \in \mathbb{Z} + \frac{1}{2}$ [97,98]. The inset in Fig. 4(b) (red dots) confirms this expectation, notably the absence of a zero-energy mode with $\ell = 0 \notin \mathbb{Z} + \frac{1}{2}$. Inserting a vortex through the center of the disk binds a Majorana zero mode there, shifts ℓ by $1/2$ such that $\ell \in \mathbb{Z}$ [97,98], and induces a second zero-energy mode on the boundary (red crosses in the inset).

Conclusion—In summary, we introduced for the first time an exactly solvable model of strongly correlated hyperbolic quantum matter, the hyperbolic Kitaev model (HKM). The non-Euclidean space-group symmetries of hyperbolic lattices play a crucial role in the model’s construction and solution. In contrast to previous noncrystalline extensions of the Kitaev model, reflection symmetries across geodesics enable an exact analytical determination of the ground-state flux sector via Lieb’s lemma, and noncommutative translation symmetries allow for an efficient determination of thermodynamic-limit properties via hyperbolic band theory. Our detailed study of the HKM on the $\{8, 3\}$ lattice reveals both Abelian and non-Abelian gapped topological spin liquids, as well as a gapless spin liquid that, unlike Kitaev’s Dirac spin liquid, has a finite low-energy density of states dominated by Majorana non-Abelian Bloch states, a unique feature of hyperbolic space.

Our Letter opens several vistas for future study. On the theoretical side, given the degree of analytical control the HKM affords, one should investigate whether the bulk hyperbolic spin liquids found here realize interesting “holographic spin liquids” on the edge [99–105]. Unlike Kitaev’s (unique) honeycomb lattice in 2D, infinitely many $\{p, 3\}$ lattices are now open to investigation, as well as other possible extensions of Kitaev physics [106–111]. On the experimental side, the spin-spin interactions in Eq. (1) could potentially be realized via qubit-photon interactions [112] in circuit quantum electrodynamics [2] with the particular spin interactions implemented using Floquet engineering [58] of Ising-type interactions [113,114]. For applications to quantum error correction, implementing a two-spin interaction in the anisotropic coupling limit $J_z \gg J_x, J_y$ might represent a simpler path towards hyperbolic surface codes than directly engineering the requisite multispin interactions [90,91,115].

Note added—While finalizing this manuscript, we became aware of an independent work [116] studying

the Kitaev model on the $\{9, 3\}$ lattice, where the authors identify a gapless chiral \mathbb{Z}_2 spin liquid.

Acknowledgments—We thank Igor Boettcher for many insightful conversations and suggestions over the course of this project, Julien Vidal for helpful feedback on several aspects of our work, as well as Marin Bukov, Felix Dusel, Juraj Hašík, Tobias Hofmann, Bastien Lapierre, Jiří Minář, Rémy Mosseri, Benedikt Placke, G. Shankar, Ronny Thomale, and Götz S. Uhrig for valuable discussions. P. M. L. acknowledges support by the European Union (ERC, QuSimCtrl, 101113633). S. D. was supported by the Faculty of Science at the University of Alberta. T. B. was supported by the Starting Grant No. 211310 by the Swiss National Science Foundation (SNSF). J. M. was supported by NSERC Discovery Grants No. RGPIN-2020-06999 and No. RGPAS-2020-00064; the Canada Research Chair (CRC) Program; and Alberta Innovates. This research was enabled in part by support provided by the Digital Research Alliance of Canada.

Views and opinions expressed are however those of the authors only and do not necessarily reflect those of the European Union or the European Research Council Executive Agency. Neither the European Union nor the granting authority can be held responsible for them.

Data availability—The data that support the findings of this Letter are openly available [117].

- [1] S. Sachdev, *Quantum Phases of Matter* (Cambridge University Press, Cambridge, England, 2023).
- [2] A. J. Kollár, M. Fitzpatrick, and A. A. Houck, Hyperbolic lattices in circuit quantum electrodynamics, *Nature (London)* **571**, 45 (2019).
- [3] P. M. Lenggenhager, A. Stegmaier, L. K. Upreti, T. Hofmann, T. Helbig, A. Vollhardt, M. Greiter, C. H. Lee, S. Imhof, H. Brand, T. Kießling, I. Boettcher, T. Neupert, R. Thomale, and T. Bzdušek, Simulating hyperbolic space on a circuit board, *Nat. Commun.* **13**, 4373 (2022).
- [4] A. Chen, H. Brand, T. Helbig, T. Hofmann, S. Imhof, A. Fritzsche, T. Kießling, A. Stegmaier, L. K. Upreti, T. Neupert, T. Bzdušek, M. Greiter, R. Thomale, and I. Boettcher, Hyperbolic matter in electrical circuits with tunable complex phases, *Nat. Commun.* **14**, 622 (2023).
- [5] W. Zhang, H. Yuan, N. Sun, H. Sun, and X. Zhang, Observation of novel topological states in hyperbolic lattices, *Nat. Commun.* **13**, 2937 (2022).
- [6] W. Zhang, F. Di, X. Zheng, H. Sun, and X. Zhang, Hyperbolic band topology with non-trivial second Chern numbers, *Nat. Commun.* **14**, 1083 (2023).
- [7] L. Huang, L. He, W. Zhang, H. Zhang, D. Liu, X. Feng, F. Liu, K. Cui, Y. Huang, W. Zhang, and X. Zhang, Hyperbolic photonic topological insulators, *Nat. Commun.* **15**, 1647 (2024).

- [8] Q. Chen, Z. Zhang, H. Qin, A. Bossart, Y. Yang, H. Chen, and R. Fleury, Anomalous and Chern topological waves in hyperbolic networks, *Nat. Commun.* **15**, 2293 (2024).
- [9] N. Balazs and A. Voros, Chaos on the pseudosphere, *Phys. Rep.* **143**, 109 (1986).
- [10] I. Boettcher, P. Bienias, R. Belyansky, A. J. Kollár, and A. V. Gorshkov, Quantum simulation of hyperbolic space with circuit quantum electrodynamics: From graphs to geometry, *Phys. Rev. A* **102**, 032208 (2020).
- [11] J. Maciejko and S. Rayan, Hyperbolic band theory, *Sci. Adv.* **7**, eabe9170 (2021).
- [12] J. Maciejko and S. Rayan, Automorphic Bloch theorems for hyperbolic lattices, *Proc. Natl. Acad. Sci. U.S.A.* **119**, e2116869119 (2022).
- [13] P. M. Lenggenhager, J. Maciejko, and T. Bzdušek, Non-Abelian hyperbolic band theory from supercells, *Phys. Rev. Lett.* **131**, 226401 (2023).
- [14] N. Cheng, F. Serafin, J. McInerney, Z. Rocklin, K. Sun, and X. Mao, Band theory and boundary modes of high-dimensional representations of infinite hyperbolic lattices, *Phys. Rev. Lett.* **129**, 088002 (2022).
- [15] E. Kienzle and S. Rayan, Hyperbolic band theory through Higgs bundles, *Adv. Math.* **409**, 108664 (2022).
- [16] Á. Nagy and S. Rayan, On the hyperbolic Bloch transform, *Ann. Henri Poincaré* **25**, 1713 (2024).
- [17] A. Attar and I. Boettcher, Selberg trace formula in hyperbolic band theory, *Phys. Rev. E* **106**, 034114 (2022).
- [18] G. Shankar and J. Maciejko, Hyperbolic lattices and two-dimensional Yang-Mills theory, *Phys. Rev. Lett.* **133**, 146601 (2024).
- [19] I. Boettcher, A. V. Gorshkov, A. J. Kollár, J. Maciejko, S. Rayan, and R. Thomale, Crystallography of hyperbolic lattices, *Phys. Rev. B* **105**, 125118 (2022).
- [20] A. Chen, Y. Guan, P. M. Lenggenhager, J. Maciejko, I. Boettcher, and T. Bzdušek, Symmetry and topology of hyperbolic Haldane models, *Phys. Rev. B* **108**, 085114 (2023).
- [21] A. J. Kollár, M. Fitzpatrick, P. Sarnak, and A. A. Houck, Line-graph lattices: Euclidean and non-Euclidean flat bands, and implementations in circuit quantum electrodynamics, *Commun. Math. Phys.* **376**, 1909 (2020).
- [22] T. Bzdušek and J. Maciejko, Flat bands and band-touching from real-space topology in hyperbolic lattices, *Phys. Rev. B* **106**, 155146 (2022).
- [23] R. Mosseri, R. Vogeler, and J. Vidal, Aharonov-Bohm cages, flat bands, and gap labeling in hyperbolic tilings, *Phys. Rev. B* **106**, 155120 (2022).
- [24] R. Mosseri and J. Vidal, Density of states of tight-binding models in the hyperbolic plane, *Phys. Rev. B* **108**, 035154 (2023).
- [25] F. R. Lux and E. Prodan, Spectral and combinatorial aspects of Cayley-crystals, *Ann. Henri Poincaré* **25**, 3563 (2024).
- [26] F. R. Lux and E. Prodan, Converging periodic boundary conditions and detection of topological gaps on regular hyperbolic tessellations, *Phys. Rev. Lett.* **131**, 176603 (2023).
- [27] S. Yu, X. Piao, and N. Park, Topological hyperbolic lattices, *Phys. Rev. Lett.* **125**, 053901 (2020).
- [28] Z.-R. Liu, C.-B. Hua, T. Peng, and B. Zhou, Chern insulator in a hyperbolic lattice, *Phys. Rev. B* **105**, 245301 (2022).
- [29] D. M. Urwyler, P. M. Lenggenhager, I. Boettcher, R. Thomale, T. Neupert, and T. Bzdušek, Hyperbolic topological band insulators, *Phys. Rev. Lett.* **129**, 246402 (2022).
- [30] Z.-R. Liu, C.-B. Hua, T. Peng, R. Chen, and B. Zhou, Higher-order topological insulators in hyperbolic lattices, *Phys. Rev. B* **107**, 125302 (2023).
- [31] Y.-L. Tao and Y. Xu, Higher-order topological hyperbolic lattices, *Phys. Rev. B* **107**, 184201 (2023).
- [32] Q. Pei, H. Yuan, W. Zhang, and X. Zhang, Engineering boundary-dominated topological states in defective hyperbolic lattices, *Phys. Rev. B* **107**, 165145 (2023).
- [33] H. Yuan, W. Zhang, Q. Pei, and X. Zhang, Hyperbolic topological flat bands, *Phys. Rev. B* **109**, L041109 (2024).
- [34] T. Tummuru, A. Chen, P. M. Lenggenhager, T. Neupert, J. Maciejko, and T. Bzdušek, Hyperbolic non-Abelian semi-metal, *Phys. Rev. Lett.* **132**, 206601 (2024).
- [35] C. Sun, A. Chen, T. Bzdušek, and J. Maciejko, Topological linear response of hyperbolic Chern insulators, *SciPost Phys.* **17**, 124 (2024).
- [36] C. Lv, R. Zhang, Z. Zhai, and Q. Zhou, Curving the space by non-Hermiticity, *Nat. Commun.* **13**, 2184 (2022).
- [37] J. Sun, C.-A. Li, S. Feng, and H. Guo, Hybrid higher-order skin-topological effect in hyperbolic lattices, *Phys. Rev. B* **108**, 075122 (2023).
- [38] K. Ikeda, S. Aoki, and Y. Matsuki, Hyperbolic band theory under magnetic field and Dirac cones on a higher genus surface, *J. Phys. Condens. Matter* **33**, 485602 (2021).
- [39] A. Stegmaier, L. K. Upreti, R. Thomale, and I. Boettcher, Universality of hofstadter butterflies on hyperbolic lattices, *Phys. Rev. Lett.* **128**, 166402 (2022).
- [40] J. B. Curtis, P. Narang, and V. Galitski, Absence of weak localization on negative curvature surfaces, *Phys. Rev. Lett.* **134**, 076301 (2025).
- [41] A. Chen, J. Maciejko, and I. Boettcher, Anderson localization transition in disordered hyperbolic lattices, *Phys. Rev. Lett.* **133**, 066101 (2024).
- [42] T. Li, Y. Peng, Y. Wang, and H. Hu, Anderson transition and mobility edges on hyperbolic lattices with randomly connected boundaries, *Commun. Phys.* **7**, 371 (2024).
- [43] M. Daniška and A. Gendiar, Analysis of quantum spin models on hyperbolic lattices and Bethe lattice, *J. Phys. A* **49**, 145003 (2016).
- [44] M. Daniška and A. Gendiar, Study of classical and quantum phase transitions on non-Euclidean geometries in higher dimensions, *Acta Phys. Slovaca* **68**, 187 (2018), <http://www.physics.sk/aps/pubs/2018/aps-18-03/aps-18-03.pdf>.
- [45] A. Götz, G. Rein, J. C. Inácio, and F. F. Assaad, Hubbard and Heisenberg models on hyperbolic lattices: Metal-insulator transitions, global antiferromagnetism, and enhanced boundary fluctuations, *Phys. Rev. B* **110**, 235105 (2024).
- [46] X. Zhu, J. Guo, N. P. Breuckmann, H. Guo, and S. Feng, Quantum phase transitions of interacting bosons on hyperbolic lattices, *J. Phys. Condens. Matter* **33**, 335602 (2021).
- [47] N. Gluscevich, A. Samanta, S. Manna, and B. Roy, Dynamic mass generation on two-dimensional electronic hyperbolic lattices, *Phys. Rev. B* **111**, L121108 (2025).

- [48] B. Roy, Magnetic catalysis in weakly interacting hyperbolic Dirac materials, *Phys. Rev. B* **110**, 245117 (2024).
- [49] A. Kitaev, Anyons in an exactly solved model and beyond, *Ann. Phys. (Amsterdam)* **321**, 2 (2006).
- [50] L. Stockmeyer, Planar 3-colorability is polynomial complete, *ACM SIGACT News* **5**, 19 (1973).
- [51] E. H. Lieb, Flux phase of the half-filled band, *Phys. Rev. Lett.* **73**, 2158 (1994).
- [52] E. H. Lieb and M. Loss, Fluxes, Laplacians, and Kasteleyn's theorem, *Duke Math. J.* **71**, 337 (1993).
- [53] N. Macris and B. Nachtergael, On the flux phase conjecture at half-filling: An improved proof, *J. Stat. Phys.* **85**, 745 (1996).
- [54] A. Jaffe and F. L. Pedrocchi, Reflection positivity for Majoranas, *Ann. Henri Poincaré* **16**, 189 (2015).
- [55] S. Chesi, A. Jaffe, D. Loss, and F. L. Pedrocchi, Vortex loops and Majoranas, *J. Math. Phys. (N.Y.)* **54**, 112203 (2013).
- [56] G. Cassella, P. d'Ornellas, T. Hodson, W. M. H. Natori, and J. Knolle, An exact chiral amorphous spin liquid, *Nat. Commun.* **14**, 6663 (2023).
- [57] S. Kim, M. Saad, D. Mao, A. Agarwala, and D. Chowdhury, Quasicrystalline spin liquid, *Phys. Rev. B* **110**, 214438 (2024).
- [58] B.-Y. Sun, N. Goldman, M. Aidelsburger, and M. Bükov, Engineering and probing non-Abelian chiral spin liquids using periodically driven ultracold atoms, *PRX Quantum* **4**, 020329 (2023).
- [59] R. Diestel, *Graph Theory*, 5th ed. (Springer, Berlin, 2017).
- [60] M. Kamfor, S. Dusuel, J. Vidal, and K. P. Schmidt, Kitaev model and dimer coverings on the honeycomb lattice, *J. Stat. Mech.* (2010) P08010.
- [61] See Supplemental Material at <http://link.aps.org-supplemental/10.1103/s25y-s4fj>, which cites additional Refs. [62–80], for a constructive proof of the existence of a symmetry-compatible three-edge coloring, derivations of Eq. (2), (4), (B2) and (B3), and technical or implementation details on the applied methods (supercell method, continued-fraction method, real-space Chern number, dispersion of chiral edge states).
- [62] D. J. S. Robinson, *A Course in the Theory of Groups*, 2nd ed. (Springer, New York, 1996).
- [63] M. Hall, Jr., *The Theory of Groups*, 2nd ed. (AMS Chelsea Publishing, Providence, 1976).
- [64] GAP, GAP—Groups, Algorithms, and Programming, Version 4.11.1, The GAP Group (2021).
- [65] J. F. Humphreys, *A Course in Group Theory* (Oxford University Press, Oxford, 1996).
- [66] X. G. Wen, F. Wilczek, and A. Zee, Chiral spin states and superconductivity, *Phys. Rev. B* **39**, 11413 (1989).
- [67] F. L. Pedrocchi, S. Chesi, and D. Loss, Physical solutions of the Kitaev honeycomb model, *Phys. Rev. B* **84**, 165414 (2011).
- [68] F. D. M. Haldane, Model for a quantum Hall effect without Landau levels: Condensed-matter realization of the “parity anomaly”, *Phys. Rev. Lett.* **61**, 2015 (1988).
- [69] J. P. Gaspard and F. Cyrot-Lackmann, Density of states from moments. Application to the impurity band, *J. Phys. C* **6**, 3077 (1973).
- [70] P. Turchi, F. Ducastelle, and G. Tréglia, Band gaps and asymptotic behaviour of continued fraction coefficients, *J. Phys. C* **15**, 2891 (1982).
- [71] C. Knetter and G. Uhrig, Perturbation theory by flow equations: Dimerized and frustrated $S = 1/2$ chain, *Eur. Phys. J. B* **13**, 209 (2000).
- [72] B. Grünbaum and G. C. Shephard, *Tilings and Patterns* (Freeman, New York, 1987).
- [73] A. W. Sandvik, Computational studies of quantum spin systems, *AIP Conf. Proc.* **1297**, 135 (2010).
- [74] J. G. Wright and B. S. Shastry, DiracQ: A quantum many-body physics package, [arXiv:1301.4494](https://arxiv.org/abs/1301.4494).
- [75] X.-G. Wen, Quantum orders in an exact soluble model, *Phys. Rev. Lett.* **90**, 016803 (2003).
- [76] H. Ebisu and B. Han, \mathbb{Z}_2 topologically ordered phases on a simple hyperbolic lattice, *Phys. Rev. Res.* **4**, 043099 (2022).
- [77] H. Yan, Hyperbolic fracton model, subsystem symmetry, and holography, *Phys. Rev. B* **99**, 155126 (2019).
- [78] H. Yan, K. Slagle, and A. H. Nevidomskyy, Y-cube model and fractal structure of subdimensional particles on hyperbolic lattices, [arXiv:2211.15829](https://arxiv.org/abs/2211.15829).
- [79] H. Yan, C. B. Jepsen, and Y. Oz, p -adic Holography from the hyperbolic fracton model, [arXiv:2306.07203](https://arxiv.org/abs/2306.07203).
- [80] N. P. Mitchell, L. M. Nash, D. Hexner, A. M. Turner, and W. T. M. Irvine, Amorphous topological insulators constructed from random point sets, *Nat. Phys.* **14**, 380 (2018).
- [81] P. M. Lenggenhager, J. Maciejko, and T. Bzdušek, HyperCells: A GAP package for constructing primitive cells and supercells of hyperbolic lattices (2023), <https://github.com/HyperCells/HyperCells>.
- [82] P. M. Lenggenhager, Emerging avenues in band theory: multigap topology and hyperbolic lattices, Ph.D. thesis, ETH Zurich, 2023, [10.3929/ethz-b-000645370](https://doi.org/10.3929/ethz-b-000645370).
- [83] M. Conder, Quotients of triangle groups acting on surfaces of genus 2 to 101, <https://www.math.auckland.ac.nz/~conder/TriangleGroupQuotients101.txt> (2007).
- [84] P. M. Lenggenhager, J. Maciejko, and T. Bzdušek, HyperBloch: A Mathematica package for hyperbolic tight-binding models and the supercell method (2023), <https://github.com/HyperCells/HyperBloch>.
- [85] R. Haydock, V. Heine, and M. J. Kelly, Electronic structure based on the local atomic environment for tight-binding bands, *J. Phys. C* **5**, 2845 (1972).
- [86] R. Haydock, V. Heine, and M. J. Kelly, Electronic structure based on the local atomic environment for tight-binding bands. II, *J. Phys. C* **8**, 2591 (1975).
- [87] J. Vidal, K. P. Schmidt, and S. Dusuel, Perturbative approach to an exactly solved problem: Kitaev honeycomb model, *Phys. Rev. B* **78**, 245121 (2008).
- [88] K. P. Schmidt, S. Dusuel, and J. Vidal, Emergent fermions and anyons in the Kitaev model, *Phys. Rev. Lett.* **100**, 057208 (2008).
- [89] A. Kitaev, Fault-tolerant quantum computation by anyons, *Ann. Phys. (Amsterdam)* **303**, 2 (2003).
- [90] N. P. Breuckmann and B. M. Terhal, Constructions and noise threshold of hyperbolic surface codes, *IEEE Trans. Inf. Theory* **62**, 3731 (2016).
- [91] N. P. Breuckmann, C. Vuillot, E. Campbell, A. Krishna, and B. M. Terhal, Hyperbolic and semi-hyperbolic surface

- codes for quantum storage, *Quantum Sci. Technol.* **2**, 035007 (2017).
- [92] A. Lavasani, G. Zhu, and M. Barkeshli, Universal logical gates with constant overhead: instantaneous Dehn twists for hyperbolic quantum codes, *Quantum* **3**, 180 (2019).
- [93] A. Jahn and J. Eisert, Holographic tensor network models and quantum error correction: A topical review, *Quantum Sci. Technol.* **6**, 033002 (2021).
- [94] O. Higgott and N. P. Breuckmann, Constructions and performance of hyperbolic and semi-hyperbolic Floquet codes, *PRX Quantum* **5**, 040327 (2024).
- [95] A. Fahimniya, H. Dehghani, K. Bharti, S. Mathew, A. J. Kollár, A. V. Gorshkov, and M. J. Gullans, Fault-tolerant hyperbolic Floquet quantum error correcting codes, [arXiv:2309.10033](https://arxiv.org/abs/2309.10033).
- [96] X. G. Wen, Mean-field theory of spin-liquid states with finite energy gap and topological orders, *Phys. Rev. B* **44**, 2664 (1991).
- [97] N. Read and D. Green, Paired states of fermions in two dimensions with breaking of parity and time-reversal symmetries and the fractional quantum Hall effect, *Phys. Rev. B* **61**, 10267 (2000).
- [98] M. Stone and R. Roy, Edge modes, edge currents, and gauge invariance in $p_x + ip_y$ superfluids and superconductors, *Phys. Rev. B* **69**, 184511 (2004).
- [99] M. Asaduzzaman, S. Catterall, J. Hubisz, R. Nelson, and J. Unmuth-Yockey, Holography on tessellations of hyperbolic space, *Phys. Rev. D* **102**, 034511 (2020).
- [100] R. C. Brower, C. V. Cogburn, A. L. Fitzpatrick, D. Howarth, and C.-I. Tan, Lattice setup for quantum field theory in AdS_2 , *Phys. Rev. D* **103**, 094507 (2021).
- [101] P. Basteiro, G. Di Giulio, J. Erdmenger, J. Karl, R. Meyer, and Z.-Y. Xian, Towards explicit discrete holography: Aperiodic spin chains from hyperbolic tilings, *SciPost Phys.* **13**, 103 (2022).
- [102] P. Basteiro, R. Nath Das, G. Di Giulio, and J. Erdmenger, Aperiodic spin chains at the boundary of hyperbolic tilings, *SciPost Phys.* **15**, 218 (2023).
- [103] P. Basteiro, F. Dusel, J. Erdmenger, D. Herdt, H. Hinrichsen, R. Meyer, and M. Schrauth, Breitenlohner-Freedman bound on hyperbolic tilings, *Phys. Rev. Lett.* **130**, 091604 (2023).
- [104] J. Chen, F. Chen, Y. Yang, L. Yang, Z. Chen, Y. Meng, B. Yan, X. Xi, Z. Zhu, G.-G. Liu, P. P. Shum, H. Chen, R.-G. Cai, R.-Q. Yang, Y. Yang, and Z. Gao, AdS/CFT correspondence in hyperbolic lattices, [arXiv:2305.04862](https://arxiv.org/abs/2305.04862).
- [105] S. Dey, A. Chen, P. Basteiro, A. Fritzsche, M. Greiter, M. Kaminski, P. M. Lenggenhager, R. Meyer, R. Sorbello, A. Stegmaier, R. Thomale, J. Erdmenger, and I. Boettcher, Simulating holographic conformal field theories on hyperbolic lattices, *Phys. Rev. Lett.* **133**, 061603 (2024).
- [106] H. Yao and S. A. Kivelson, Exact chiral spin liquid with non-Abelian anyons, *Phys. Rev. Lett.* **99**, 247203 (2007).
- [107] S. Yang, D. L. Zhou, and C. P. Sun, Mosaic spin models with topological order, *Phys. Rev. B* **76**, 180404 (2007).
- [108] H. Yao, S.-C. Zhang, and S. A. Kivelson, Algebraic spin liquid in an exactly solvable spin model, *Phys. Rev. Lett.* **102**, 217202 (2009).
- [109] C. Wu, D. Arovas, and H.-H. Hung, Γ -matrix generalization of the Kitaev model, *Phys. Rev. B* **79**, 134427 (2009).
- [110] M. Barkeshli, H.-C. Jiang, R. Thomale, and X.-L. Qi, Generalized Kitaev models and extrinsic non-Abelian twist defects, *Phys. Rev. Lett.* **114**, 026401 (2015).
- [111] A. Vaezi, \mathbb{Z}_3 generalization of the Kitaev's spin-1/2 model, *Phys. Rev. B* **90**, 075106 (2014).
- [112] P. Bienias, I. Boettcher, R. Belyansky, A. J. Kollár, and A. V. Gorshkov, Circuit quantum electrodynamics in hyperbolic space: From photon bound states to frustrated spin models, *Phys. Rev. Lett.* **128**, 013601 (2022).
- [113] Y. Salathé, M. Mondal, M. Oppliger, J. Heinsoo, P. Kurpiers, A. Potočnik, A. Mezzacapo, U. Las Heras, L. Lamata, E. Solano, S. Filipp, and A. Wallraff, Digital quantum simulation of spin models with circuit quantum electrodynamics, *Phys. Rev. X* **5**, 021027 (2015).
- [114] L. B. Nguyen, Y. Kim, A. Hashim, N. Goss, B. Marinelli, B. Bhandari, D. Das, R. K. Naik, J. M. Kreikebaum, A. N. Jordan, D. I. Santiago, and I. Siddiqi, Programmable Heisenberg interactions between Floquet qubits, *Nat. Phys.* **20**, 240 (2024).
- [115] A. Jahn, M. Gluza, F. Pastawski, and J. Eisert, Majorana dimers and holographic quantum error-correcting codes, *Phys. Rev. Res.* **1**, 033079 (2019).
- [116] F. Dusel, T. Hofmann, A. Maity, Y. Iqbal, M. Greiter, and R. Thomale, Chiral gapless spin liquid in hyperbolic space, [arXiv:2407.15705](https://arxiv.org/abs/2407.15705).
- [117] P. M. Lenggenhager, S. Dey, T. Bzdušek, and J. Maciejko, Supplementary data and code for: Hyperbolic Spin Liquids (2025), [10.5281/zenodo.14439718](https://doi.org/10.5281/zenodo.14439718).

End Matter

Appendix A: Symmetric 3-edge coloring—The three edges coincident on a vertex of the $\{2m, 3\}$ lattice are in one-to-one correspondence with the three sides of a face of the dual $\{3, 2m\}$ lattice, which is an equilateral triangle [see white or gray triangles in Fig. 1(a), for $m = 4$]. Those three sides belong to distinct equivalence classes under reflections in the sides of any equilateral triangle, which are bond-cutting reflection symmetries of the original $\{2m, 3\}$ lattice. By coloring the sides of the equilateral triangles according to their equivalence class,

we obtain a three-edge coloring which respects those reflection symmetries and allows us to use Lieb's lemma.

Mathematically, the edges of the $\{2m, 3\}$ lattice form the right coset space $H \backslash G$ where the hyperbolic triangle group $G = \Delta(2, 3, 2m)$ is the space group of the $\{2m, 3\}$ lattice [19,20] and H is the subgroup of G which leaves a given edge invariant (stabilizer subgroup). Further quotienting out reflections in the sides of the equilateral triangles, which form the subgroup $K = \Delta(m, m, m)$ of G , we obtain the double coset space $H \backslash G / K$ which contains only three

elements, i.e., three colors. For computations using hyperbolic band theory the chosen Bravais unit cell or supercell must be compatible with this edge coloring. This is ensured if the corresponding translation group Γ is a normal subgroup of both G and K . In Sec. I of the Supplemental Material [61], we spell out the above mathematical arguments in more rigor.

Appendix B: Majorana hyperbolic band theory—The generic quadratic Majorana Hamiltonian $\hat{\mathcal{H}} = \frac{1}{4} \sum_{j,k} A_{jk} \hat{c}_j \hat{c}_k$ with $A^\top = -A$ and $\{\hat{c}_j, \hat{c}_k\} = 2\delta_{jk}$ defined on a hyperbolic lattice with translation group Γ can be written in reciprocal space [11,12] using the generalized Fourier transform [35]

$$\hat{a}_{\mu\nu,j}^{(K)} = \frac{1}{\sqrt{2|\Gamma|}} \sum_{\gamma \in \Gamma} \sqrt{d_K} \hat{c}_{\gamma,j} D_{\nu\mu}^{(K)}(\gamma), \quad (\text{B1})$$

where K runs over all irreducible representations (IRs) $D^{(K)}$ and μ, ν run from 1 to d_K , the dimension of $D^{(K)}$. Defining $iA^{(K)} = \sum_{\gamma \in \Gamma} iA(\gamma) \otimes D^{(K)}(\gamma)$, we obtain

$$\hat{\mathcal{H}} = \frac{i}{2} \sum_K \sum_{\mu,\nu,\nu'} \sum_{j,k} A_{\nu,j;\nu',k}^{(K)} \hat{a}_{\mu\nu,j}^{(K)\dagger} \hat{a}_{\mu\nu',k}^{(K)}. \quad (\text{B2})$$

Diagonalizing the Hermitian matrices $iA^{(K)}$, giving operators $\hat{d}_{\mu\lambda,l}^{(K)}$ and eigenvalues $\varepsilon_{\lambda,l}(K)$, finally results in

$$\hat{\mathcal{H}} = \sum_{\substack{K,\lambda,\mu,l \\ \varepsilon_{\lambda,l}(K)>0}} \varepsilon_{\lambda,l}(K) \left(\hat{d}_{\mu\lambda,l}^{(K)\dagger} \hat{d}_{\mu\lambda,l}^{(K)} - \frac{1}{2} \right). \quad (\text{B3})$$

Analogously to the Euclidean case, the sum is constrained to positive energies due to the reality of the Majorana fermions, which relates states corresponding to conjugate IRs. The derivation of Eq. (B2) and (B3) amounts to straightforward algebraic manipulations, see Supplemental Material [61], Sec. IV.

Appendix C: Extrapolation using the supercell method—The supercell method [13] provides a framework for including the effect of higher-dimensional IRs $D^{(K)}$ by sampling one-dimensional IRs on successively larger unit cells (supercells). To estimate the *true* value of a given quantity, we compute it for supercell sizes $N \in \{1, 4, 16, 32, 128\}$ (see Supplemental Material [61], Sec. V) and subsequently extrapolate N to ∞ . Below, we discuss the details of this procedure for the ground-state (GS) energy and for the fermionic spectral gap.

The GS energy is given by $E_0 = -\frac{1}{4} |\varepsilon_{\lambda,l}(K)|$ with the average running over the full spectrum. On the n th supercell, we randomly sample N_s momenta from the corresponding Abelian Brillouin zone $ABZ^{(n)}$ and compute

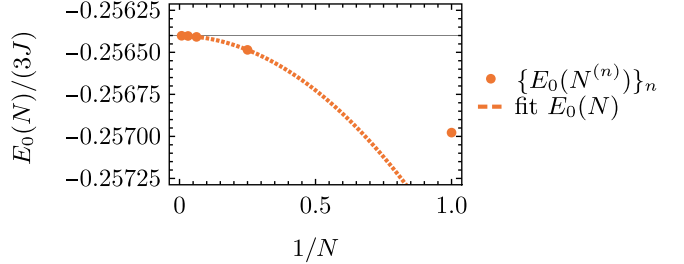


FIG. 5. Extrapolation of the ground-state energy $E_0(N)$ for the homogeneous π -flux configuration. The data points show the values obtained using Eq. (C1) and the line is the fit according to Eq. (C2) (excluding $n = 1$). We find $E_0/(3J) = -0.25640(1 \pm 6)$ from a fit with coefficient of determination $1 - R^2 \sim 10^{-12}$.

$$E_0(N^{(n)}) = -\frac{1}{4N_s} \sum_{\mathbf{k} \in ABZ^{(n)}, l} |\varepsilon_l(\mathbf{k})|. \quad (\text{C1})$$

We extrapolate using a weighted least-squares fit with model

$$E_0(N) = E_0 + \frac{u}{N} + \frac{v}{N^2}, \quad (\text{C2})$$

and weights N , excluding the primitive cell $n = 1$. In Fig. 5, we demonstrate this for the homogeneous π -flux configuration. The resulting estimate for E_0 is given together with the parameter error reflecting a 95% confidence interval.

The spectral gap $\Delta E = 2E_g$ is the extent of the interval of energies $[-E_g, E_g]$ with vanishing density of states (DOS). We estimate ΔE through the integrated DOS

$$\mathcal{N}(E, N) = \int_0^E dE' \rho(E', N), \quad (\text{C3})$$

obtained by constructing a cumulative histogram of the computed eigenvalues. It shows a transition between the region $E < E_g$ where $\mathcal{N}(E, N)$ is suppressed for increasing N and the region $E > E_g$ where it is enhanced, see Figs. 6(a) and 6(b). The extrapolation of $\mathcal{N}(E, N)$ simultaneously takes into account the effects due to non-Abelian Bloch states and finite sampling of Abelian Bloch states without being overly sensitive to the chosen energy resolution (due to the integration).

Using a maximum-likelihood algorithm (see Supplemental Material [61], Sec. V C), we fit $\mathcal{N}(E, N)$ as a function of $1/N$ (for $N > 1$) in the vicinity of E_g using the linearized model

$$\mathcal{N}(E, N) = \mathcal{N}_0(E) + \frac{s(E)}{N}, \quad (\text{C4})$$

and weights N to account for the larger weight of non-Abelian states in larger supercells. Some examples of fits are shown in Fig. 6(b). From each fit, we extract \mathcal{N}_0 and the slope s together with their 95% confidence intervals,

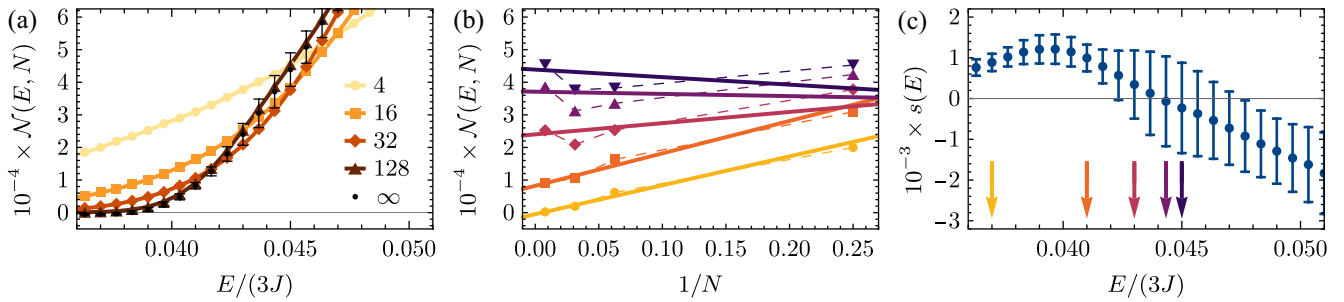


FIG. 6. Estimation of the spectral gap. Integrated density of states $\mathcal{N}(E, N)$ for $J_x = J_y = J_z = J$ and $K/(3J) = 0.1$. (a) $\mathcal{N}(E, N)$ as a function of energy E for different supercells (see inset legend for the supercell size N), including the extrapolated value $\mathcal{N}_0(E)$ (“ $N = \infty$ ”) with 95% confidence intervals shown as error bars. (b) $\mathcal{N}(E, N)$ as a function of the inverse supercell size $1/N$ for the values of energy indicated by the correspondingly colored arrows in panel (c). Dashed lines are guides to the eye and the solid lines are linear maximum-likelihood fits. (c) The slope $s(E)$ extracted from the same fits as a function of energy E ; error bars indicate 95% confidence intervals.

see Figs. 6(a) and 6(c), respectively. The extrapolated integrated DOS $\mathcal{N}_0(E)$ is expected to change from 0 to a positive value at E_g . On the other hand, the slope $s(E)$ is expected to change its sign from positive below E_g to negative above. From both datasets, we obtain estimates of E_g including uncertainties due to the confidence intervals. Results with combined uncertainties are shown in Fig. 3 as a function of J_z and K (see also Supplemental Material [61], Sec. VII B).

For sufficiently large ΔE , this reduces to finding the intersection of $\mathcal{N}(E)$ for the largest two supercells. We employed this computationally more efficient approach to obtain the full phase diagrams in Figs. 2(a) and 4(a).

Appendix D: Ground-state flux sector—To verify that the ground-state flux sector is indeed the homogeneous π -flux configuration both for $K = 0$ and $K \neq 0$, we study the ground-state energy E_0 in different flux sectors. For computational reasons, we restrict the analysis to translation-invariant flux configurations with no net flux per unit cell. Since a primitive cell has six faces and the number of plaquettes with $W_P = -1$ has to be even, there are $2^{6-1} = 32$ such configurations, reducing to six equivalence classes by symmetry. The results are shown in Fig. 7 for $K = 0$ and $K/(3J) = 1/6$ (see also Supplemental Material [61], Sec. VII A for extended figures).

Appendix E: Chiral edge states—To extract the dispersion $E(\ell)$ of the edge states in the chiral phase, plotted in Fig. 4(b), we assign to each eigenstate $|\psi_n\rangle$ of the Majorana Hamiltonian on a circular flake two quantities: (i) degree of localization near the edge $p_{n,\text{edge}}$, and (ii) angular momentum ℓ_n . We define the first as $p_{n,\text{edge}} = \sum_{j \in \text{edge}} |\psi_n(j)|^2$, where “ $j \in \text{edge}$ ” indicates sites located within the outer 10% of the hyperbolic distance to the boundary. The computed values exhibit a sharp jump in p_{edge} at energies $E/(3J) \approx \pm 0.6$, see Fig. 4(b).

Because of the discrete rotation symmetry, ℓ_n is defined only modulo 8. However, since low-energy states have a wavelength much larger than the lattice spacing, we anticipate the emergence of an unbounded ℓ near $E = 0$. In the continuum limit, the eigenvalue ℓ is associated with $e^{i\ell\varphi}$, where the phase of the wave function grows with angular coordinate φ . Therefore, $c_{n,\ell} = |\sum_{j \in \text{sites}} e^{-2i\ell\varphi(j)} \psi_n^2(j)| \in [0, 1]$ estimates the probability that $|\psi_n\rangle$ carries angular momentum $\ell \in \mathbb{Z}/2$. The computed values $c_{n,\ell}$ are dominated by a single branch, $\ell = \ell_n$. The branch has approximately linear dispersion $E(\ell)$, with $\ell \in \mathbb{Z}$ ($\ell \in \mathbb{Z} + \frac{1}{2}$) in the absence (presence) of a vortex at the center of the disk as shown in Fig. 4(b). For technical details, see Supplemental Material [61], Sec. X.

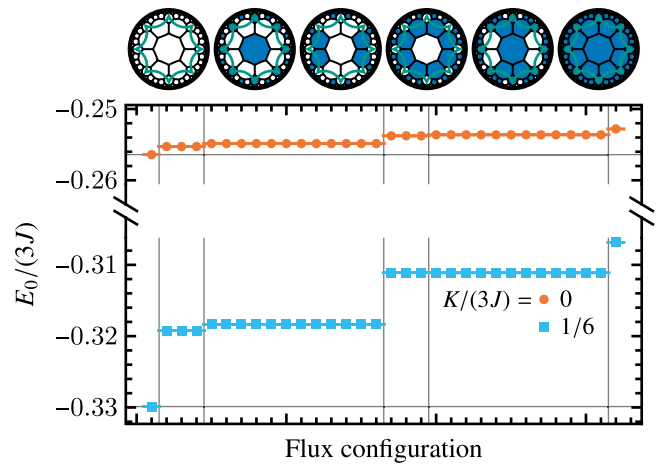


FIG. 7. Ground-state energy for the 32 translation-invariant flux configurations with zero net flux per unit cell for $J_x = J_y = J_z = J$ and different values of K (see legend). Error bars indicate 95% confidence intervals. The flux configurations fall into the six equivalence classes (separated by the vertical gray lines) shown at the top with white (blue shaded) octagons denoting plaquettes with π (0) flux. In both cases, the homogeneous π -flux configuration has lowest energy.